

Opposed Jet Flames of Lean or Rich Premixed Propane-Air Reactants versus Hot Products

JOSEPH A. WEHRMEYER,* ZHONGXIAN CHENG, DAVID M. MOSBACHER, and ROBERT W. PITZ

Mechanical Engineering Department, Vanderbilt University Box 1592 Station B, Nashville, TN 37235, USA

and

ROBIN OSBORNE

ERC, Inc., NASA Marshall Space Flight Center, Huntsville, AL 35812, USA

Several opposed jet flames, produced by a lean H₂-air jet opposing a rich or lean C₃H₈-air jet, are investigated. Spontaneous Raman spectroscopy is used for major species concentration and temperature measurements along the opposed jet centerline. The hot products of the H₂-air flame simulate the burnt gases of strong-burning near-stoichiometric reactants as they impinge upon a weak-burning lean or rich hydrocarbon-fueled reactant mix, a situation encountered in stratified charge operation of direct injection spark ignition engines. In addition the H₂-air flame hot products facilitate experimental data interpretation through the absence of carbon-bearing species. Good agreement between numerical and experimental data are obtained for a rich (equivalence ratio, $\phi = 1.25$) C₃H₈-air jet versus a lean ($\phi = 0.4$) H₂-air jet. Two lean C₃H₈-air jets ($\phi = 0.64$ or 0.60), versus the $\phi = 0.4$ H₂-air jet, are also investigated. For both of these flames, the amount of CO₂ production strongly depends upon ϕ , with the $\phi = 0.64$ flame having a peak CO₂ mole fraction an order of magnitude higher than for the $\phi = 0.60$ flame, and the C₃H₈ flames burning either as a normal flame (high CO₂) or as a "negative flame speed" flame producing little CO₂ and then only through diffusion of C₃H₈ into the hot products jet. The numerically predicted and experimental CO₂ profiles agree well for the positive flame speed flame, but the large discrepancy between predicted and measured peak CO₂ in the negative flame speed flame suggests modeling improvements are needed for this type of flame. © 2002 by The Combustion Institute

INTRODUCTION

The opposed jet burner is an invaluable tool for examining the interplay among chemical reaction, diffusion, and convection processes occurring in premixed [1], non-premixed (pure diffusion) [2], or partially premixed laminar flames [3, 4]. Measurements of temperature and major species concentrations have been made in opposed jet flames using intrusive thermocouple and gas sampling probes as well as, more recently, non-intrusive laser-based methods [1, 2, 4]. The experimental data can be compared to numerical results obtained from a finite-differencing solution of the flowfield's conservation equations along the burner symmetry axis. The solution is obtained by solving a two-point boundary value problem involving a set of ordinary differential equations that are derived from the original partial differential equations

via a similarity transformation [5]. The widely available CHEMKIN Collection [6] contains a software application, Oppdif, that uses the methods of Reference 5 to model-opposed jet premixed and/or diffusion flames.

The present work seeks to investigate the structure of partially premixed C₃H₈-air flames produced in an opposed jet burner, where reactant jets of disparate and very lean or very rich stoichiometry impinge upon each other. These types of flames are related to the combustion processes occurring in a stratified charge, spark-ignited internal combustion engine, where a flame located in a region of burnable stoichiometry may support a region that is so lean or rich that it is near (or beyond) the limit of being able to support combustion.

The stratified charge direct injection spark ignition (DISI) engine has recently been introduced on a widespread commercial scale in both Japan and Europe for use in automobiles. A benefit of the DISI engine is its fuel efficiency relative to the typical port-injected spark igni-

*Corresponding author. E-mail: wehrme@vuse.vanderbilt.edu

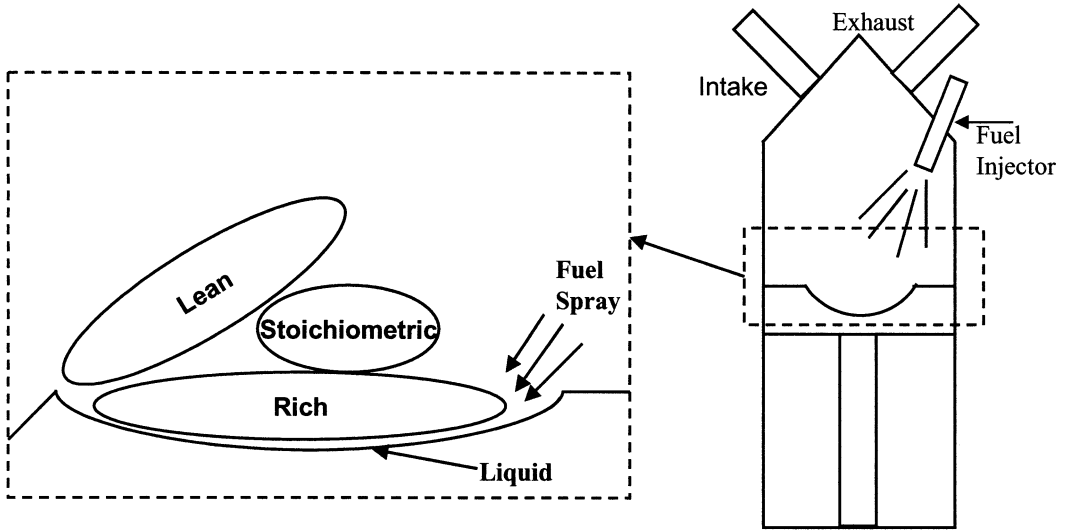


Fig. 1. Schematic of stratified charge operation of DISI engine.

tion engine at idle or light load operation, mainly because of the elimination of the air throttle and its concomitant pressure losses [7]. At light load conditions the DISI engine operates in a stratified charge mode, which is conceptually shown in Fig. 1. In this mode the fuel is directly injected into the combustion chamber during the compression stroke and hence has time to mix with only a portion of the air in the chamber. As a result a burnable mixture does not exist throughout the chamber. Instead, regions exist within the chamber where there are mixtures either too lean or possibly even too rich to burn.

The DISI engine has not yet seen use in North America because of emissions regulations. While the problem of concurrent NO_x and O_2 in the exhaust may be overcome with lean- NO_x catalysts or a conventional catalyst coupled with a NO_x storage “bank,” another problem to overcome is the amount of hydrocarbon (HC) emissions produced under stratified charge operation. These HC emissions occur because the regions of very lean or very rich stoichiometry do not support complete combustion, and the fuel located in these regions is not fully transformed into combustion products. Thus a better understanding of combustion phenomena, occurring when a flame from a region of burnable mixture supports reaction in regions either too lean or too rich to burn, is

needed. In addition to stoichiometry, other factors influence the ability of a mixture to burn. These factors include aerodynamic strain rate and flame curvature, both of which are shown to influence flame extinction [8, 9].

The interaction between reacting flows of disparate equivalence ratio can be fundamentally modeled by two counterflowing jets of premixed reactants, as shown in Fig. 2. Each jet can be rich or lean, even outside of flammability limits (as understood in the typical sense of a freely propagating flame). To investigate combustion processes similar to those occurring in

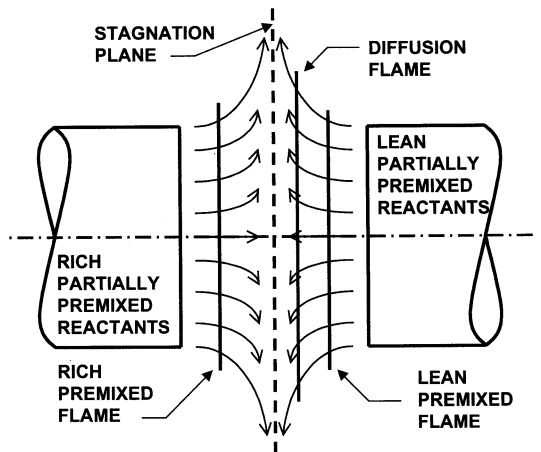


Fig. 2. Opposed jet burner schematic, showing a “triple flame.”

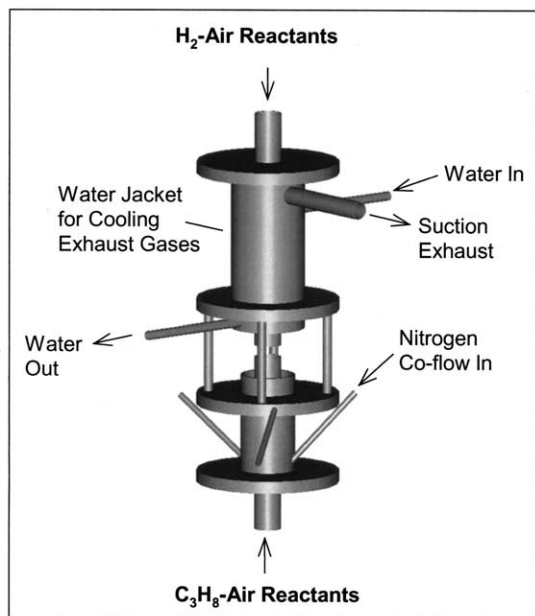


Fig. 3. Opposed jet burner schematic showing co-flow, exhaust, and water cooling.

stratified charge DISI engines, one can investigate counterflow partially premixed flames where one jet is stoichiometric (or rich or lean) and impinges upon a lean or rich jet. These situations correspond to those shown on the left of Fig. 1, where the stoichiometric (or slightly rich or lean but burnable) region impinges upon either a lean or rich region that is unburnt and

may even be incapable of burning except by the sustaining action provided by the hot products of the burnt region.

MATERIALS AND METHODS

Experimental Methodology

Figure 3 shows a schematic of the opposed jet burner used in this work, and is similar to the opposed jet burner of Reference 3. Straight nozzles of 25 mm diameter are separated from each other by a distance of 12.5 mm. A series of screens (together with glass beads in the bottom nozzle) inhibit the formation of boundary layers along the nozzles' walls, providing "top hat" velocity profiles that have as nozzle exit boundary conditions: zero radial velocity and zero axial velocity gradient. Nitrogen co-flow around the bottom nozzle, coupled with exhaust vacuum around the top nozzle, reduce the mixing of nozzle reactants with surrounding quiescent air. Cooling of the hot exhaust products by a water jacket between the annular exhaust and the inner jet prevents preheating of the reactants coming from the top nozzle.

Figure 4 shows the optical setup used for the opposed jet burner. Visible laser Raman spectroscopy is used to measure temperature and species concentrations of the major reactants

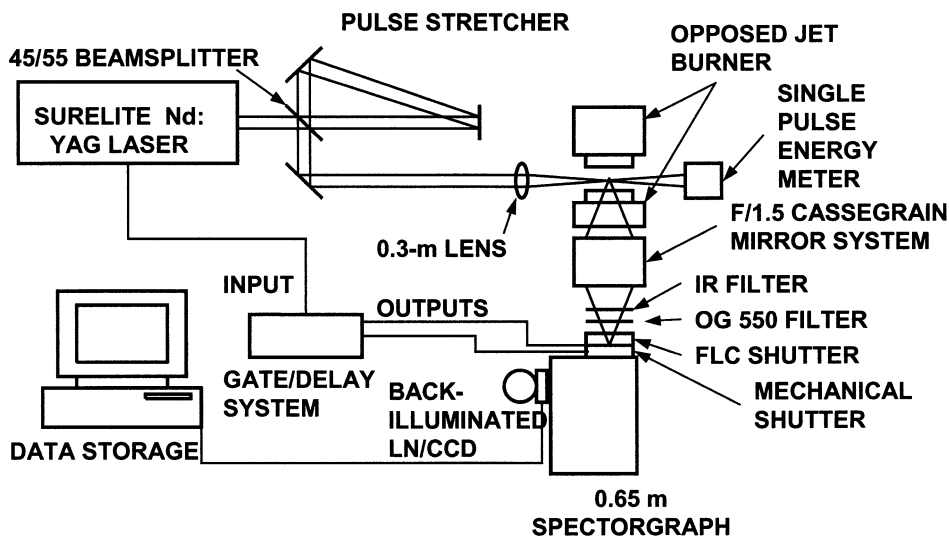


Fig. 4. Laser system schematic.

and products. The Raman signals are created by passing a 90 mJ laser beam through the burner and focusing it using a 0.3 m lens to improve spatial resolution transverse to the laser beam direction. The beam waist (the spatial resolution of the Raman measurements) is 0.3 mm. The laser is a 532 nm frequency-doubled, pulsed Nd-YAG laser, capable of 400 mJ per pulse. However, only 90 mJ enters the sample volume, because half of the beam energy passes through a beamsplitter (not shown) and is used to pump a dye laser for other experiments, and additional beam losses occur through the use of a mirrors-beamsplitter arrangement (pulse stretcher) that lengthens the effective pulse length from 10 ns to ~ 30 ns. This is done to prevent laser-induced breakdown from occurring at the laser focus.

The Raman scattered light is collected at 90° to the laser beam by an F/1.5 Cassegrain mirror system and focused onto the slit of a 0.65 m spectrograph. The light detector is a liquid nitrogen (LN) cooled, back-illuminated CCD array, allowing simultaneous measurement of Raman signals from all major species. To minimize the amount of 532 nm light entering the spectrograph, a 2 mm thick OG550 color-glass filter is mounted at the entrance slit. An infrared filter is also used to prevent infrared stray light in the spectrograph from interfering with the visible Raman signals. The LN CCD has its own mechanical shutter, but is relatively slow at opening and closing, with a minimum effective open time of ~ 30 ms. Rather than use this mechanical shutter, another faster mechanical shutter with a 6 ms effective open time is used at the entrance slit of the spectrometer. This mechanical shutter is synchronized to the firing of the laser to be open during the laser pulse and then to close, significantly blocking out time-continuous background flame luminosity coming from the flame. However not all of the flame luminosity is blocked, since there is still some that enters the spectrometer during the 6 ms shutter open time. A ferro-electric liquid crystal (FLC) shutter is also used in series with the mechanical shutter. The exposure time for the FLC is ~ 40 μ s but the "light leakage" characteristic of the FLC still requires the simultaneous use of the mechanical shutter [10]. Using this optical setup, a Raman spectrum is ob-

tained at each of several locations along the 12.5 mm separation distance of the nozzles. The opposed jet burner is mounted on a translation stage to move it with respect to the optical system. The experimental results are derived from the Raman measurements through an experimental calibration of the Raman system. The calibration process involves obtaining Raman measurements in several calibration flames produced in a "Hencken" multielement, adiabatic flat-flame diffusion burner, substituted for the opposed jet burner. Measured total number density is related to temperature via the ideal gas law, assuming atmospheric pressure.

Typical uncertainties (based on photon shot noise calculations) for flame temperature measurements range approximately from $\pm 2\%$ to $\pm 7\%$. Uncertainties for mole fraction measurements range approximately from $\pm 3\%$ for all species in lean flames, up to $\pm 35\%$ for the small CO mole fraction measurements in rich flames. These uncertainties are functions of both the net wavelength-integrated Raman signal strength and the amount of background interference that must be subtracted to obtain a net Raman signal. Background interference is due to both continuous flame luminosity (corrected by subtracting an image obtained with the laser off from the Raman image obtained with the laser on) and laser-induced background (corrected by subtracting an interference amount determined by the laser-induced background on both sides of a Raman signal). Representative uncertainty error bars are shown in the graphs of experimental data for each temperature or mole fraction profile.

Figure 5 shows a set of Raman spectra obtained from one of the three opposed jet flames described in the following section. Each spectrum is the result of a 20 s accumulation of light signals (200 laser pulses from the 10 Hz laser) onto the CCD, and each spectrum has background luminosity subtracted. In Fig. 5 one of the four spectra (position 4.25 mm) is obtained in the region between a rich premixed C_3H_8 -air flame and a diffusion flame. At this location, the strong background luminosity, after subtraction, results in a net spectrum with more noise than for other locations, as shown by the increased random noise present in the spectrum for position 4.25 mm compared to other positions.

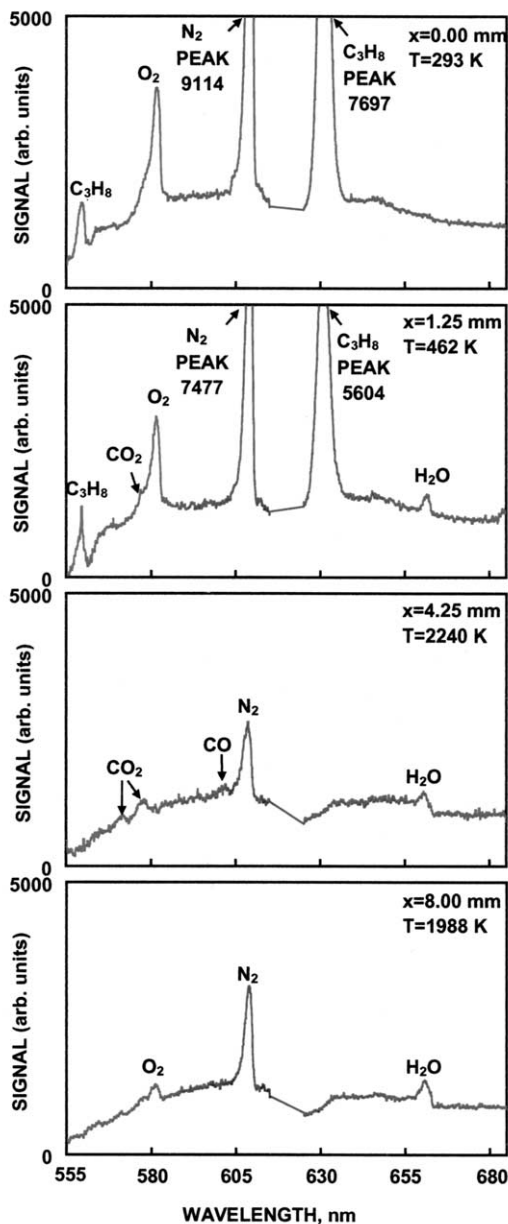


Fig. 5. Set of Raman spectra obtained in partially premixed opposed jet flame: C₃H₈-air ($\phi = 1.25$) versus H₂-air ($\phi = 0.4$). Strain rate = 180 s⁻¹. Positions: 0.00 mm in cold C₃H₈-air reactants, 1.25 mm in C₃H₈-air premixed flame, 4.25 mm between C₃H₈-air premixed and diffusion flames, 8.00 mm in H₂-air products. 615–625 nm not imaged.

Flames Examined

As previously mentioned, in a stratified charge DISI engine, a strongly burning, near-stoichiometric region can support reaction of a weakly

burning region that is either fuel-rich or fuel-lean. Three opposed jet flames, fundamentally similar to the stratified combustion occurring in a DISI engine, are analyzed in this work. Each of the three flames has a jet of lean (equivalence ratio, $\phi = 0.4$) H₂-air premixed reactants impinging upon a jet of premixed C₃H₈-air reactants. One flame has rich C₃H₈-air reactants, another has lean C₃H₈-air reactants, and the third has very lean C₃H₈-air reactants, so lean in fact that a premixed C₃H₈-air flame does not exist. Propane, a relatively simple hydrocarbon compared to gasoline, *n*-heptane, or isoctane, is chosen as the fuel because it is easy to work with, existing as a gas at atmospheric pressure, and its combustion chemistry has been modeled by others [11], yet it possesses some of the characteristics of higher-order hydrocarbon combustion, such as chemical reactions involving species bearing multiple C atoms.

For one of the jets, lean H₂-air reactants are used rather than C₃H₈-air reactants, for two reasons. Firstly, H₂'s fast flame speed allows the premixed flame for this jet to be almost completely independent of the premixed and/or diffusion flames created by the C₃H₈-air jet; thus strain rate effects on just the C₃H₈-air jet can be determined. Secondly, no carbon-bearing species exist in the H₂-air jet, and as a result the CO₂ or CO that is measured can be attributed solely to the reactants coming from the C₃H₈-air jet. This is of benefit when examining highly strained “negative flame speed” C₃H₈-air flames, one of which is described below.

A strain rate for each of the flames is estimated from the following equation which can be used to describe a “global” strain rate, a , based on the opposed jet boundary conditions [12]:

$$a = (2 u_1/L) (1 + (\rho_1 u_1^2/\rho_2 u_2^2)^{1/2})$$

where L is the separation distance between the opposed nozzles, and ρ_i and u_i are the density and exit velocity for nozzle i , with $i = 1$ arbitrarily chosen as the H₂ nozzle and $i = 2$ the C₃H₈ nozzle. Exit velocities and densities are determined from experimental mass flowmeter measurements, assuming uniform exit flow.

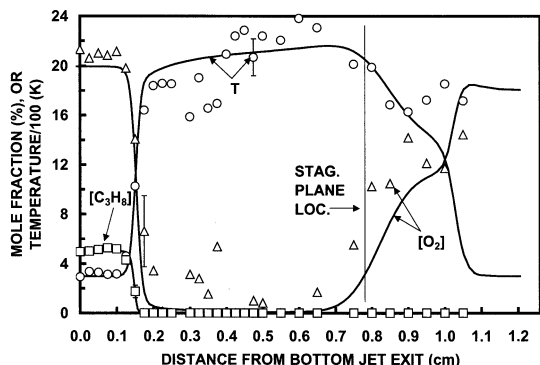


Fig. 6. Experimental and numerically predicted product profiles for a partially premixed opposed jet flame. C_3H_8 -air ($\phi = 1.25$) versus H_2 -air ($\phi = 0.4$). Experimental strain rate = 180 s^{-1} . Numerical data shifted by 0.5 mm.

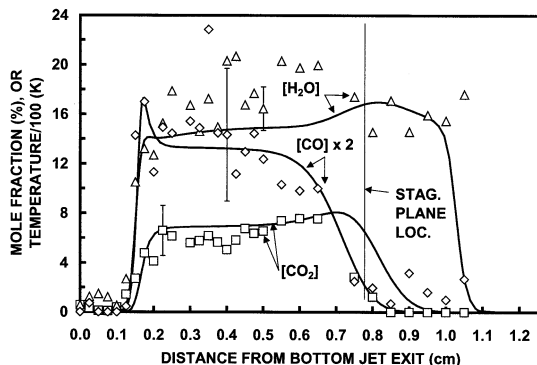


Fig. 7. Experimental and numerically predicted product profiles for a partially premixed opposed jet flame. C_3H_8 -air ($\phi = 1.25$) versus H_2 -air ($\phi = 0.4$). Experimental strain rate = 180 s^{-1} . Numerical data shifted by 0.5 mm.

Reaction Mechanism

The C_3H_8 -air combustion chemistry model used is the “M5” mechanism [11] and the molecular transport processes are modeled using the standard transport data in CHEMKIN. The M5 mechanism is a modified version of the Warnatz alkane combustion mechanism [13]. Reactions involving $n-C_3H_7$ are not included in the M5 mechanism to make it computationally faster. To offset the absence of $n-C_3H_7$, modifications of rate data are made specifically to the reaction converting $i-C_3H_7$ to C_3H_6 and to several fuel-breakdown steps (making them irreversible) that create $i-C_3H_7$. The deletion of the $n-C_3H_7$ reactions, coupled with the rate changes to the $i-C_3H_7$ production/destruction reactions, allows the M5 mechanism to predict unstrained laminar C_3H_8 -air flame speeds within $\sim 5\%$ of those predicted with the Warnatz mechanism, but with much less computational time required [11]. This computational speed is required to model turbulent combustion in DISI engines, and hence the M5 mechanism is also chosen as the chemistry model for this work.

RESULTS AND DISCUSSION

Rich C_3H_8 Flame versus Hot Products

Figure 6 shows experimental and numerical temperature and reactant concentrations data in a partially premixed flame ($a = 180\text{ s}^{-1}$)

where a rich ($\phi = 1.25$) C_3H_8 -air jet impinges upon the hot products coming from a lean H_2 -air flame. The experimental and numerical data are in good agreement in Fig. 6, and are also in good agreement in Fig. 7 (which shows combustion product concentrations) except that the experimental CO_2 profile is narrower than the numerically predicted CO_2 profile. The extra width for the numerically predicted CO_2 profile occurs in the diffusion flame region of this “triple flame.” It is possible that the numerical results, because of either the chemistry model or the transport model, do not properly predict the overall rate of transformation of CO into CO_2 for this region, where O_2 diffusing from the H_2 -air products is needed for the transformation. To facilitate comparison of the widths and peak values for the experimental and numerical profiles, the numerical data has been shifted toward the left (toward the C_3H_8 -air nozzle) by 0.5 mm. This is the difference between the numerically predicted location for the C_3H_8 premixed flame and the experimentally measured location. This small discrepancy could be because of errors in initial positioning of the laser with respect to the bottom nozzle location and to partial burning of the H_2 -air jet in its nozzle (described below) which would increase the momentum flux exiting that nozzle. The stagnation plane location, shown in Figs. 6 and 7, is based upon the shifted numerical results.

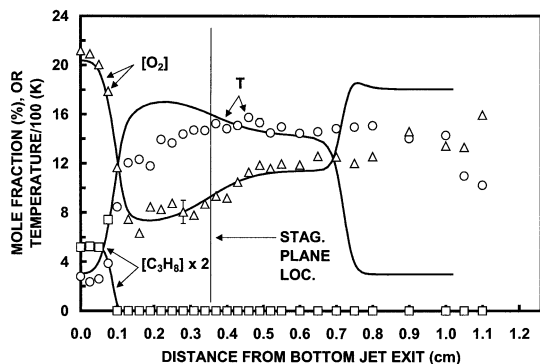


Fig. 8. Experimental and numerically predicted product profiles for a partially premixed opposed jet flame. C_3H_8 -air ($\phi = 0.64$) versus H_2 -air ($\phi = 0.4$). Experimental strain rate = 140 s^{-1} . Numerical data shifted by 2.4 mm.

Lean, "Positive Flame Speed" C_3H_8 Flame versus Hot Products

Figures 8 and 9 show data for a lean ($\phi = 0.64$) C_3H_8 -air reactant jet impinging upon the H_2 -air jet. The numerical data show the H_2 -air flame existing off of the boundary, however, the experimental data, with high temperatures and high H_2O values measured all the way to the H_2 -air jet nozzle, show that the H_2 -air flame is anchored near the nozzle exit. This anchoring is probably the result of the retaining ring which keeps the last screen mounted inside of the top nozzle. A recirculation zone caused by this ring allows the lean H_2 -air flame to be attached near the top nozzle. The experimental data also show the existence of a premixed C_3H_8 flame, with

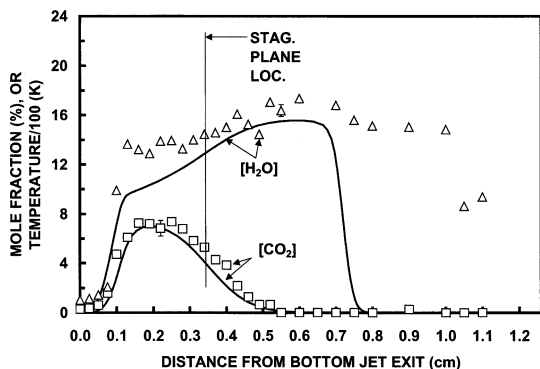


Fig. 9. Experimental and numerically predicted product profiles for a partially premixed opposed jet flame. C_3H_8 -air ($\phi = 0.64$) versus H_2 -air ($\phi = 0.4$). Experimental strain rate = 140 s^{-1} . Numerical data shifted by 2.4 mm.

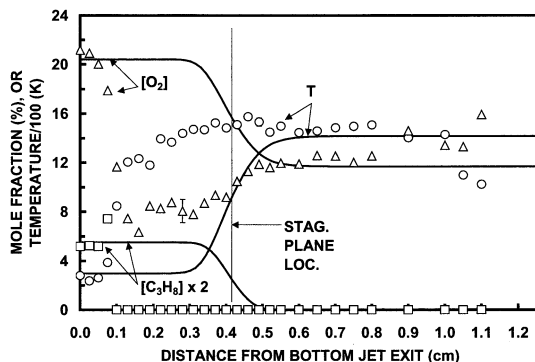


Fig. 10. Experimental and numerically predicted product profiles for a partially premixed opposed jet flame. C_3H_8 -air ($\phi = 0.64$) versus H_2 -air ($\phi = 0.4$). Experimental strain rate = 390 s^{-1} . Numerical boundary conditions and experimental strain rate assume H_2 -air reacts in nozzle. Experimental data same as in Fig. 8.

the experimental CO_2 profile rising to a peak value of $\sim 8\%$, and the experimental O_2 profile dipping to a minimum value of $\sim 7\%$, which is lower than the $\sim 12\%$ value for excess O_2 in the H_2 -air jet after combustion. Likewise the numerical data, using a cold reactants boundary condition for the H_2 -air jet boundary, also show the same general trends as the experimental data in the premixed C_3H_8 -air flame region. The numerical O_2 and CO_2 profiles match well to the experimental profiles in the C_3H_8 -air premixed flame region, and match relatively well in the diffusion zone around the stagnation plane, except to its left side. At that location (around 0.2 cm), the measured temperatures are low and the measured H_2O mole fractions are high when compared to the simulations.

To bracket the effect that the anchored H_2 -air flame has upon the C_3H_8 -flame, another set of numerical results is generated using the H_2 -air boundary condition that assumes complete and adiabatic combustion of the reactants before exiting the nozzle. This increases both the temperature and velocity of the H_2 -air combustion products exiting the nozzle, with the velocity rising from the normal unreacted velocity (47 cm/s) by approximately the ratio of temperature increase, which is $\sim 1,400/300$ (giving 205 cm/s). The numerical results with this new boundary condition are compared to experimental data (the same experimental data as in Figs. 8 and 9) in Figs. 10 and 11. At this higher

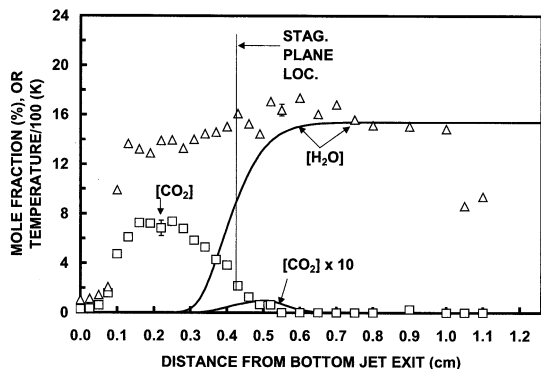


Fig. 11. Experimental and numerically predicted product profiles for a partially premixed opposed jet flame. C_3H_8 -air ($\phi = 0.64$) versus H_2 -air ($\phi = 0.4$). Experimental strain rate = 390 s^{-1} . Numerical boundary conditions and experimental strain rate assume H_2 -air reacts in nozzle. Experimental data same as in Fig. 9.

strain rate condition, the premixed C_3H_8 flame is predicted to be nonexistent, and instead the only C_3H_8 combustion occurs via diffusion of that fuel into the hot products of the H_2 -air jet, and as a result the peak CO_2 concentration is predicted on the H_2 -air side of the stagnation plane (see Fig. 11). Because of this lack of a premixed C_3H_8 flame, the numerically predicted peak CO_2 concentration is very low compared to that of a premixed flame. In Fig. 11, the numerically predicted CO_2 profile is magnified by a factor of ten to be discernable, since its peak CO_2 value is only $\sim 0.1\%$. This is almost two orders of magnitude less than what is experimentally measured; thus a definite premixed C_3H_8 flame, occurring to the C_3H_8 side of the stagnation plane, is being measured. This shows the cold H_2 -air reactants boundary condition is the more appropriate one to use (compared to the complete reaction boundary condition) when examining the premixed C_3H_8 flame and diffusion zone (around the stagnation plane) regions, even though that boundary condition is different from what actually exists at the H_2 -air jet nozzle.

Considering the fact that the experimental temperature and H_2O profiles both drop near the H_2 -air jet nozzle, the H_2 -air flame probably exists very near, although not inside of, the nozzle, and thus the best boundary condition with which to model the experimental data would be one with temperature, velocity, and

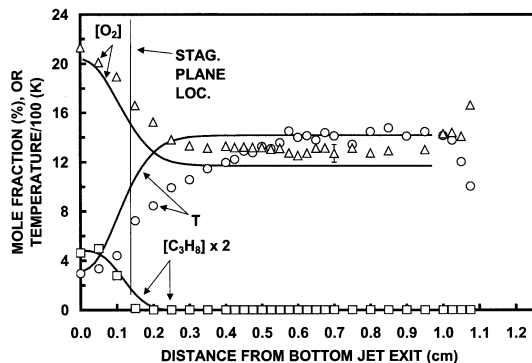


Fig. 12. Experimental and numerically predicted product profiles for a partially premixed opposed jet flame. C_3H_8 -air ($\phi = 0.60$) versus H_2 -air ($\phi = 0.4$). Experimental strain rate = 390 s^{-1} . Numerical boundary conditions and experimental strain rate assume H_2 -air reacts in nozzle. Numerical data shifted by 2.9 mm.

species related to some partial degree of reaction having occurred for the H_2 -air reactants, rather than assuming either absolutely none or complete reaction. However no direct exit velocity measurements were obtained for this work. Instead, exit velocities were related to mass flowmeter measurements and nozzle dimensions. Raman data could not be obtained extremely close to the H_2 -air nozzle because of excessive elastic light scattering off the nozzle wall. For Figs. 10 and 11, no attempt is made to shift the numerical data for better comparison to the experimental data, since the experimental data are for a premixed C_3H_8 -air flame, existing on the C_3H_8 side of the stagnation plane, while the numerical data are for a diffusion-controlled C_3H_8 flame existing on the H_2 -air side of the stagnation plane. These two types of flames have been referred to as “positive flame speed flames” and “negative flame speed flames,” respectively [14, 15].

Lean, “Negative Flame Speed” C_3H_8 Flame versus Hot Products

Figures 12 and 13 show data for a lean C_3H_8 -air jet ($\phi = 0.60$) impinging upon the H_2 -air jet. The difference between this flame and the previous one is a slight decrease in the C_3H_8 -air jet stoichiometry. This slight decrease is enough to prevent a C_3H_8 -air premixed flame from existing at this strain rate. Now the only chem-

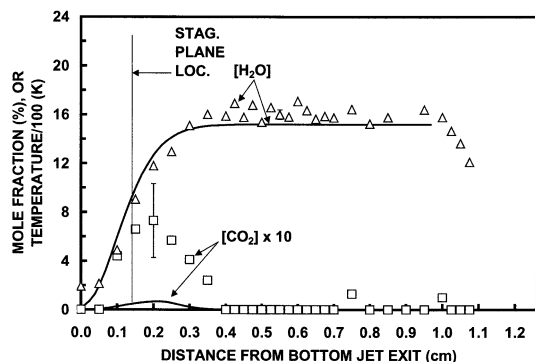


Fig. 13. Experimental and numerically predicted product profiles for a partially premixed opposed jet flame. C_3H_8 -air ($\phi = 0.60$) versus H_2 -air ($\phi = 0.4$). Experimental strain rate = 390 s^{-1} . Numerical boundary conditions and experimental strain rate assume H_2 -air reacts in nozzle. Numerical data shifted by 2.9 mm.

ical reaction occurring for the C_3H_8 is in the diffusion zone between the C_3H_8 -air jet and the hot products of the H_2 -air flame; in other words a negative flame speed flame exists. In the diffusion zone around the stagnation plane the temperature is sufficient to allow the C_3H_8 that can diffuse across the stagnation plane to react with the excess, hot O_2 at that location. This situation is analogous to the DISI stratified charge operation where a combustion chamber region too lean to burn interfaces with a region of burned gases. The numerically predicted CO_2 profile, while similar in extent to the experimental profile, is almost an order of magnitude less in peak value than for the experimental profile. The H_2 -air boundary condition used for this flame is the same as for Figs. 10 and 11, where complete reaction of the H_2 and air is assumed to occur inside the nozzle, with a resulting high temperature and high velocity occurring at the nozzle exit. The numerical data are shifted by 2.9 mm to facilitate comparison with experimental data.

The peak CO_2 value and its location with respect to the stagnation plane are sensitive to strain rate (boundary velocity) for a negative flame speed flame, with the peak value dropping and moving closer toward the stagnation plane with increasing strain rate [16]. In addition the reactant and temperature profiles become steeper across the diffusion zone (which contains the stagnation plane) as strain rate in-

creases. Because the experimental data show less steep temperature and reactant profiles than do the numerical data, as well as have a higher peak CO_2 profile than do the numerical data, it would appear that the velocity for the H_2 -air jet boundary condition should be reduced. However even using the cold, unreacted boundary velocity (47 cm/s) instead of the hot, reacted boundary velocity (205 cm/s) for the H_2 -air jet, the new numerically predicted CO_2 mole fraction profile (not shown) has a peak value that is still significantly less (0.2% compared to 0.7%) than the experimentally measured peak CO_2 mole fraction.

In addition to the M5 mechanism, another C_3H_8 -air reaction mechanism was used [17] in an effort to achieve better agreement between experimental and numerical peak CO_2 mole fraction values for this flame. Both reaction mechanisms were found to produce essentially the same numerical results, for this $\phi = 0.60$ C_3H_8 -air flame as well as for the other two flames.

The order-of-magnitude discrepancy between peak CO_2 experimental and numerical data in Fig. 13 cannot be attributed to experimental uncertainty, since there is excellent agreement across the entire CO_2 experimental and numerical profiles for the positive flame speed flame of Fig. 9, even in regions with CO_2 mole fractions values similar to the peak experimental value of Fig. 13. This suggests that lean, strained, low temperature C_3H_8 -air combustion processes, especially those involved with the diffusional transport and combustion of C_3H_8 in negative flame speed flames, are inadequately modeled. This may be because of the chemistry mechanism, but also may be because of the transport mechanism. Proper modeling of the diffusive transport process is especially critical for negative flame speed flames, where combustion occurs only by the diffusive transport of C_3H_8 across the stagnation plane and into the hot jet.

SUMMARY AND CONCLUSIONS

Several opposed jet flames, produced by a jet of lean H_2 -air reactants opposing a jet of rich or lean C_3H_8 reactants, are investigated both nu-

merically and experimentally. Through the use of spontaneous Raman spectroscopy, major species concentration and temperature measurements are obtained at several locations along the opposed jet centerline. The hot products of the H₂-air flame, in addition to facilitating experimental data interpretation through the absence of carbon-bearing species, also simulate the burnt gases of strong-burning near-stoichiometric reactants as they impinge upon a weak-burning very lean or rich reactant mixture. Good agreement between numerical and experimental data is (except for CO₂ in the diffusion flame region) obtained for a rich ($\phi = 1.25$) C₃H₈-air jet versus a lean ($\phi = 0.4$) H₂-air jet. This provides confidence that the "M5" model is adequate for this type of rich reactants versus hot products opposed jet flame. However, discrepancies arise when comparing the numerical and experimental data for the very lean C₃H₈-air jet ($\phi = 0.60$) versus the same H₂-air reactant jet, where the lean C₃H₈ jet is near the lean limit for freely propagating flame combustion. For the $\phi = 0.6$ C₃H₈-air flame, there is only a small amount of CO₂ detected, indicating a negative flame speed flame exists. However the experimentally measured peak CO₂ value is several times larger than that numerically predicted, indicating the combustion model, and/or the molecular transport model, even though adequate to model near-stoichiometric C₃H₈ combustion and even rich C₃H₈-air combustion, may need improvement in modeling very lean positive flame speed or negative flame speed combustion. These are the types of combustion processes that need to be modeled accurately to predict the amount of fuel burnout and unburnt hydrocarbon production in DISI engines.

The authors would like to acknowledge the U.S. Department of Energy's Office of Basic Energy Sciences who have supported this work through a Partnerships for Academic-Industrial Research, PAIR, grant (#DE-FG02-98ER14915, with Dr. Alan H. Laufer as Technical Monitor). The authors also wish to acknowledge the helpful interactions of Michael Drake of the General Motors Research Institute and Volker Sick of the University of Michigan.

REFERENCES

1. Law, C. K., and Sung, C. J., *Prog. Energy Comb. Sci.* 26:459 (2000).
2. Brown, T. M., Tanoff, M. A., Osborne, R. J., Pitz, R. W., and Smooke, M. D., *Combust. Sci. and Tech.* 129:71 (1997).
3. Seshadri, K., Puri, I., and Peters, N., *Combust. Flame* 61:237 (1985).
4. Tanoff, M. A., Smooke, M. D., Osborne, R. J., Brown, T. M., and Pitz, R. W., *Twenty-Sixth Symposium (International) on Combustion*, The Combustion Institute, Pittsburgh, 1996, pp. 1121–1128.
5. Kee, R. J., Miller, J. A., and Evans, G. H., *Twenty-Second Symposium (International) on Combustion*, The Combustion Institute, Pittsburgh, 1988, pp. 1479.
6. Kee, R. J., Rupley, F. M., Miller, J. A., Coltrin, M. E., Grcar, J. F., Meeks, E., Moffat, H. K., Lutz, A. E., Dixon-Lewis, G., Smooke, M. D., Warnatz, J., Evans, G. H., Larson, R. S., Mitchell, R. E., Petzold, L. R., Reynolds, W. C., Caracotsios, M., Stewart, W. E., and Glarborg, P., CHEMKIN Collection, Release 3.5, Reaction Design, Inc., San Diego, CA (1999).
7. Takagi, Y., *Twenty-Seventh Symposium (International) on Combustion*, The Combustion Institute, Pittsburgh, 1998, pp. 2055–2068.
8. Law, C. K., *Twenty-Second Symposium (International) on Combustion*, The Combustion Institute, Pittsburgh, 1988, pp. 1381–1402.
9. Choi, C. W., and Puri, I. K., *Combust. Flame* 123:119 (2000).
10. Wehrmeyer, J. A., Yeralan, S., and Tecu, K. S., *Opt. Lett.* 20:934 (1995).
11. Haworth, D. C., Blint, R. J., Cuenot, B., and Poinso, T. J., *Combust. Flame* 121:395 (2000).
12. Kim, J. S., Libby, P. A., and Williams, F. A., *Comb. Sci. Tech.* 87:1 (1992).
13. Warnatz, J., *Eighteenth Symposium (International) on Combustion*, The Combustion Institute, Pittsburgh, 1981, pp. 369–384.
14. Sohrab, S. H., Ye, Z. Y., and Law, C. K., *Twentieth Symposium (International) on Combustion*, The Combustion Institute, Pittsburgh, 1984, pp. 1957–1965.
15. Gran, I. R., Echehki, T., Chen, J. H., *Twenty-Sixth Symposium (International) on Combustion*, The Combustion Institute, Pittsburgh, 1996, pp. 323–329.
16. Darabiha, N., Candel, S. M., Marble, F. E., *Combust. Flame* 64:203 (1986).
17. Sung, C. J., Li, B., Wang, H., and Law, C. K., *Twenty-Seventh Symposium (International) on Combustion*, The Combustion Institute, Pittsburgh, 1998, pp. 1523–1529.

Received 31 May 2001; revised 17 September 2001; accepted 14 October 2001